Results in Physics 44 (2023) 106156

Contents lists available at ScienceDirect

Results in Physics

journal homepage: www.elsevier.com/locate/rinp

Pressure-induced phase transition and band-gap decrease in semiconducting $Na_3Bi(IO_3)_6$

Robin Turnbull [a,*], Javier González-Platas [b], Akun Liang [a], Dequan Jiang [c], Yonggang Wang [c], Catalin Popescu [d], Plácida Rodríguez-Hernández [e], Alfonso Muñoz [e], Jordi Ibáñez [f], Daniel Errandonea [a]

[a] Departamento de Física Aplicada - Instituto de Ciencia de Materiales, MALTA Consolider Team, Universidad de Valencia, Edificio de Investigación, C/Dr. Moliner 50, Burjassot, 46100 Valencia, Spain
[b] Departamento de Física - Instituto Universitario de Estudios Avanzados en Física Atómica, Molecular y Fotónica (IUDEA), MALTA Consolider Team, Universidad de La Laguna, Avenida Astrofísico Fco. Sánchez s/n, La Laguna, Tenerife, E-38204, Spain
[c] Center for High Pressure Science and Technology Advanced Research, Beijing 100094, China
[d] CELLS-ALBA Synchrotron Light Facility, 08290 Cerdanyola del Vallès, Barcelona, Spain
[e] Departamento de Física, Instituto de Materiales y Nanotecnología, MALTA Consolider Team, Universidad de La Laguna, La Laguna, E-38204 Tenerife, Spain
[f] Geosciences Barcelona (GEO3BCN-CSIC), MALTA Consolider Team, 08028 Barcelona, Spain

ARTICLE INFO

Keywords:
Matter at extreme conditions
New materials
Phase transitions
High pressure
Synchrotron X-ray diffraction

ABSTRACT

We report a combined experimental/theoretical high-pressure study of $Na_3Bi(IO_3)_6$ under compression to 11.2 GPa at ambient temperature. Through a combination of single-crystal and powder synchrotron X-ray diffraction, optical absorption measurements and *ab initio* density functional theory calculations we unambiguously show a first-order pressure-induced phase transition at around 9.5 GPa from the ambient pressure phase, referred to here as α-$Na_3Bi(IO_3)_6$, to a new crystalline structure referred to here as β-$Na_3Bi(IO_3)_6$. The triclinic (P-1) to triclinic (P1) phase transition is characterised by a doubling of the primitive cell volume, whereby the crystallographic b-axis doubles in length, and by a decrease in the volume per formula unit of approximately 3 %. The phase transition is also characterised by an indirect → indirect electronic bandgap decrease of approximately 0.1 eV as measured by absorption spectroscopy (3.44(1) → 3.32(1) eV) and calculated via density functional calculations (2.48 → 2.33 eV). We also report the pressure evolution of the crystal lattice parameters and isothermal compressibility tensor of the ambient pressure phase α-$Na_3Bi(IO_3)_6$, which reveals highly anisotropic compressibility and a bulk modulus of 30.4(7) GPa.

Introduction

Iodate materials exhibit a wide variety of chemical compounds and structural polymorphs due to the variety of possible I^{5+} coordination configurations. Typically, the I^{5+} cation adopts a three- or four-coordinated configuration, resulting in IO_3^- and IO_4^- fundamental units respectively. The IO_3^- unit possesses a lone electron pair (LEP), making it electrically polar, which leads to interesting and valuable macroscopic anisotropic effects in IO_3^- materials such as: photocatalysis, second harmonic generation (SHG) and optical birefringence [1–4]. The anisotropic properties can be enhanced by combining the IO_3^- unit with other chemical species which have LEPs, such as the Bi^{3+} cation, and in fact bismuth iodates have been shown to have strong non-linear properites [5,6]. Recently the alkali metal bismuth iodate $Na_3Bi(IO_3)_6$ was synthesised with the specific aim of exploring the effect of high pressure on the optical bandgap [7]. This compound has been shown to exhibit a highly intriguing crystal structure, with one-dimensional BiI_6O_{18} chains that strongly affect the optical response both at ambient pressure and as a function of pressure. However, much work remains to be done in order to fully understand how high pressure affects the optical and structural properties of $Na_3Bi(IO_3)_6$ and, in particular, to determine the crystal structure of the high-pressure phases. In the present work, we investigate the compression behaviour of the alkali metal bismuth iodate $Na_3Bi(IO_3)_6$ by single crystal and powder X-ray diffraction, single crystal optical absorption measurements and *ab initio* density functional theory calculations.

* Corresponding author.
E-mail address: robin.turnbull@uv.es (R. Turnbull).

https://doi.org/10.1016/j.rinp.2022.106156
Received 19 October 2022; Received in revised form 29 November 2022; Accepted 2 December 2022
Available online 5 December 2022

Methods

Sample preparation

Submillimetre pale-yellow single crystals of $Na_3Bi(IO_3)_6$ were synthesised following the hydrothermal method of Ref. 7. The precursors, 0.351 g (6 mmol) of NaCl (Shanghai Aladdin Biochemical Technology Co., ltd, 99.0 %), 1.283 g (6 mmol) of $NaIO_4$ (Sinopharm Chemical Reagent Co., ltd, 99.0 %), 0.466 g (1 mmol) of Bi_2O_3 (Sinopharm Chemical Reagent Co., ltd, 99.9 %), 1.368 g (6 mmol) of H_5IO_6 (Sinopharm Chemical Reagent Co., ltd, 99.9 %), and 3 ml H_2O were sealed in a 25 ml Teflon-lined autoclave. The autoclave was then heated to 230 °C and held at this temperature for 4 days. After those 4 days, the autoclave was cooled slowly to room temperature at a rate of 5 ∘C/h to obtain the single crystals. The crystals can be seen in Supplementary Fig. 1 in addition to a Le Bail fit of polycrystalline diffraction data acquired at ambient conditions. Polycrystalline $Na_3Bi(IO_3)_6$ samples were prepared by grinding the aforementioned single crystals in a pestle and mortar for 10 min under a 4:1 methanol-ethanol mixture.

Measurements

Angle-dispersive single-crystal XRD data were acquired in the X-ray Diffraction Service (SIDIX) at the University of La Laguna. CrysAlisPro [8] was used to collect, index, scale and apply numerical absorption corrections to the data. Single crystal diffraction measurements (SC-XRD) were performed at room temperature using a Rigaku SuperNOVA diffractometer equipped with an EOS CCD detector and Mo radiation micro-source (λ = 0.71073 Å). All measurements were processed with the CrysAlisPro software version 1.171.40.71 (Ref. 8). Numerical absorption correction based on Gaussian integration over a multifaceted crystal model was applied using the ABSORB-7 program[9]. For HP measurements we used a Mini-Bragg DAC from Almax-EasyLab, with an opening angle of 85∘ and anvil culets of 500 μm diameter, fitted with a stainless-steel gasket containing a hole of 200 μm diameter and 75 μm depth. A 4:1 methanol-ethanol (ME) mixture was used as PTM[10]. The sample was placed on one of the diamonds anvils (diffracted side) together with a small ruby sphere as pressure sensor[11]. The structure was refined, for each pressure, using previous results as starting point, on F^2 by full-matrix least-squares refinement using the SHELXL program [12].

Polycrystalline XRD data were acquired at ALBA Synchrotron[13] (Barcelona, Spain) on the BL04 - MSPD beamline at using a monochromatic beam λ = 0.4246 Å focused to a spot size of 20 × 20 μm. A SX165 Rayonix Mar CCD detector was used to record the data.

The optical absorption spectra were acquired using the sample-in sample-out method on the in-house optical set-up at the University of Valencia, consisting of: a visible-near IR spectrometer (Ocean Optics Maya2000 Pro), a tungsten filament lamp, fused silica lenses and reflecting optical objectives. The intensity of the light transmitted through the sample ($I(\omega)$) was normalised against the intensity of the light transmitted through the 16:3:1 methanol-ethanol–water PTM ($I_0(\omega)$). Single crystals of $Na_3Bi(IO_3)_6$, approximately 100 × 100 × 40 μm^3 in size, were loaded into membrane driven DACs with culet sizes of 500 μm. Tungsten gaskets were pre-indented to 50 μm thickness, then sample chambers 250 μm in diameter were drilled prior to loading the crystals. Ruby crystals were included in sample chamber for use as a pressure gauge. The indirect bandgap energies at different pressures were determined via Tauc plot analysis of the absorption spectra[14], wherein for each spectrum a linear fit of the high-energy part of the $(\alpha)^{1/2}$ vs $h\upsilon$ plot is interpolated to the x-axis, (i.e. zero absorption,) where α is the absorption coefficient, h is Planck's constant, and υ is the photon frequency.

Equations of state (EoS) were fitted to the volume-pressure data using EosFit7-GUI[15] whereby the EoS were constrained to second or third-order Birch-Murnaghan equations[16,17].

Ab initio density functional theory calculations

The simulations of the different crystalline phases of $Na_3Bi(IO_3)_6$ were calculated within the framework of density-functional theory (DFT)[18], using the Vienna Ab-initio Simulation Package (VASP) [19,20] to perform simulations with the projector augmented-wave (PAW)[21,22] scheme including the following configurations for Bi ($5d^{10}6s^26p^3$), I ($5\ s^2\ 5p^5$), O ($2\ s^2\ 2p^4$), and Na ($2p^6\ 3\ s^1$) pseudopotentials. Accurate convergence of the total energy, stress, and forces was achieved with a plane-wave cut-off of 540 eV. The exchange–correlation energy was described with the generalized-gradient approximation (GGA) functional with the Armiento-Mattsson prescription (AM05) [23,24]. The sampling of the Brillouin-zone (BZ) was performed with Monkhorst-Pack[25] grids of 4 × 4 × 2 and 4 × 2 × 2 for the low (α) and high (β) pressure phases respectively.

For each volume (pressure) structural relaxations were performed on the experimentally determined crystal structures allowing the cell parameters and the atomic positions to change during the relaxation until the forces on atoms are lower than 0.003 eV/Å and the stress diagonal tensor is isotropic and converged to below 0.1 GPa. From our simulations we obtain a set of volume, energy, and pressure data that can be fitted using a third-order Birch-Murnaghan[16] EOS to obtain the equilibrium volume, bulk modulus, and the pressure derivative. To provide insights regarding thermodynamic stability of the analysed phase for increasing pressure we compare the enthalpy curves ($H = E + PV$).

The electronic band structures were obtained with the VASP package. For these calculations the k-path was chosen with the SeeK-path package[26].

Results and discussion

Crystal structure

Until the present work, $Na_3Bi(IO_3)_6$ had only been investigated at high pressure conditions via infra-red and Raman spectroscopy, which, according to Ref. 7, indicated two pressure-induced phase transitions, at 1.9 and 8.2 GPa, based on the (dis)appearance/splitting of vibrational modes. In this work we use single crystal and powder synchrotron X-ray diffraction data to confirm the higher-pressure phase transition (∼ 9 GPa) and we solve the high-pressure structure for the first time. The XRD data, combined with the single crystal absorption data, also show that no phase transition occurs at lower pressure, which contradicts the findings of Ref. 7. The findings of Ref. 7 are rationalised in terms of the high-pressure response of the PTM. The higher-pressure phase transition (∼ 9 GPa) is also characterised bandgap closure of ∼ 0.1 eV according to both experiment and *ab initio* density functional calculations.

The crystal structures of the low-pressure α-$Na_3Bi(IO_3)_6$ and the new high-pressure β-$Na_3Bi(IO_3)_6$ polymorphs were confirmed/determined based on single-crystal XRD data as discussed in this paragraph. Refinement of experimental single crystal XRD data unambiguously confirms that, at ambient pressure and temperature, $Na_3Bi(IO_3)_6$ crystallizes in the triclinic (P-1) crystal system as determined in the initial publication to report the synthesis of this compound[7]. This ambient pressure structure, herein referred to as α-$Na_3Bi(IO_3)_6$, is shown in Fig. 1 a. The ambient pressure diffraction data were integrated with a very low R_{int} = 0.0264 for 3848 unique reflections. Details of the XRD data collection and refinement for α-$Na_3Bi(IO_3)_6$ are provided in Supplementary Tables 1-5. With increasing pressure, the single crystal XRD results reveal that no phase transition takes place until between 8.8 and 9.5 GPa wherein α-$Na_3Bi(IO_3)_6$ exhibits a first order phase transition (from P-1 to P1). The pressure induced transition from α-$Na_3Bi(IO_3)_6$ to the new high pressure phase, herein referred to as β-$Na_3Bi(IO_3)_6$ (shown in Fig. 1b), is characterised by a doubling of the primitive cell volume, (because the b-axis doubles in length, becoming the new c-axis,) and by a decrease in the volume per formula unit of approximately 3 %. The new

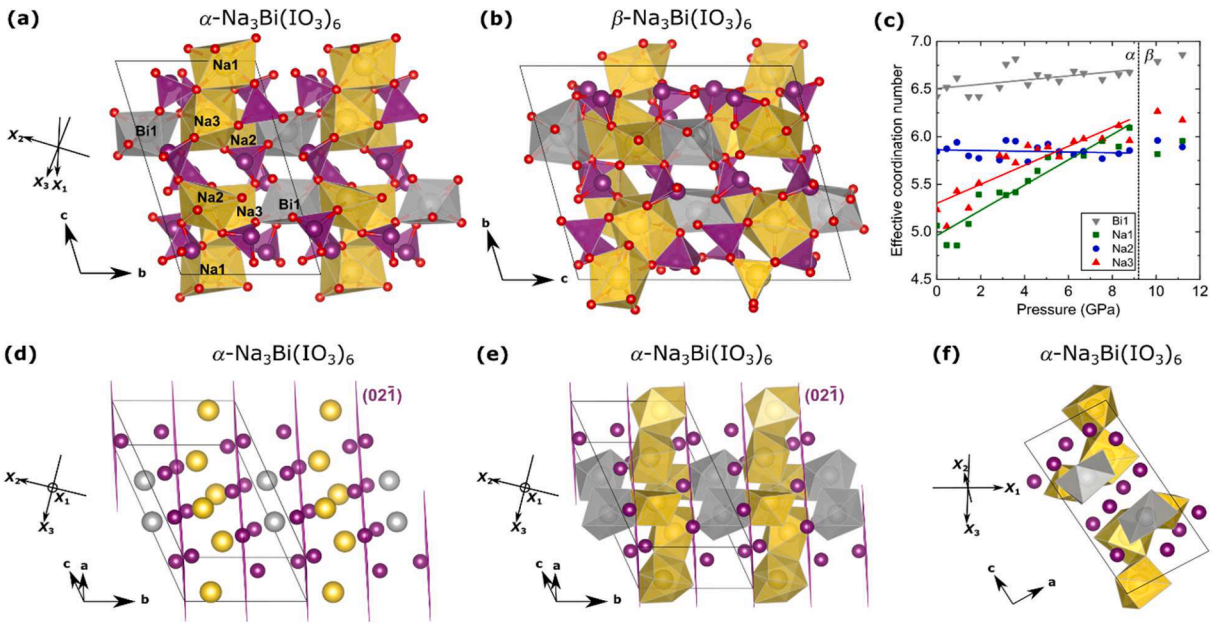

Fig. 1. Crystal structures of $Na_3Bi(IO_3)_6$ determined from single crystal XRD. (a) The low pressure structure: α-$Na_3Bi(IO_3)_6$. (b) The high pressure structure: β-$Na_3Bi(IO_3)_6$. (c) The pressure-induced evolution of the effective coordination number of the NaO_x and BiO_x polyhedra according to Vesta[27]. The atoms Na1, Na2 Na3 and Bi1 are labelled in Fig. 1a. In the β- phase, the Na and Bi atoms are all unique, therefore the average effective coordination for the corresponding polyhedra is shown. (d, e) The α-phase projected along the axis of major compression, X_1, clearly displaying the layered structure. (f) The α-phase projected with the X_1 compression axis parallel to the page (pointing from left to right). Yellow/Grey/Purple/Red spheres represent Na/Bi/I/O atoms. The principal compression axes (X_1, X_2 and X_3) are shown for α-$Na_3Bi(IO_3)_6$. The X_1 compression axis is twice as compressible as X_2 and X_3. The crystal structures were rendered in Vesta[27]. Supplementary crystallographic data for both α-and β-$Na_3Bi(IO_3)_6$ structures can be obtained free of charge from the Cambridge Crystallographic Data Centre (CCDC) under deposition numbers 2162824–2162844. (For interpretation of the references to colour in this figure legend, the reader is referred to the web version of this article.)

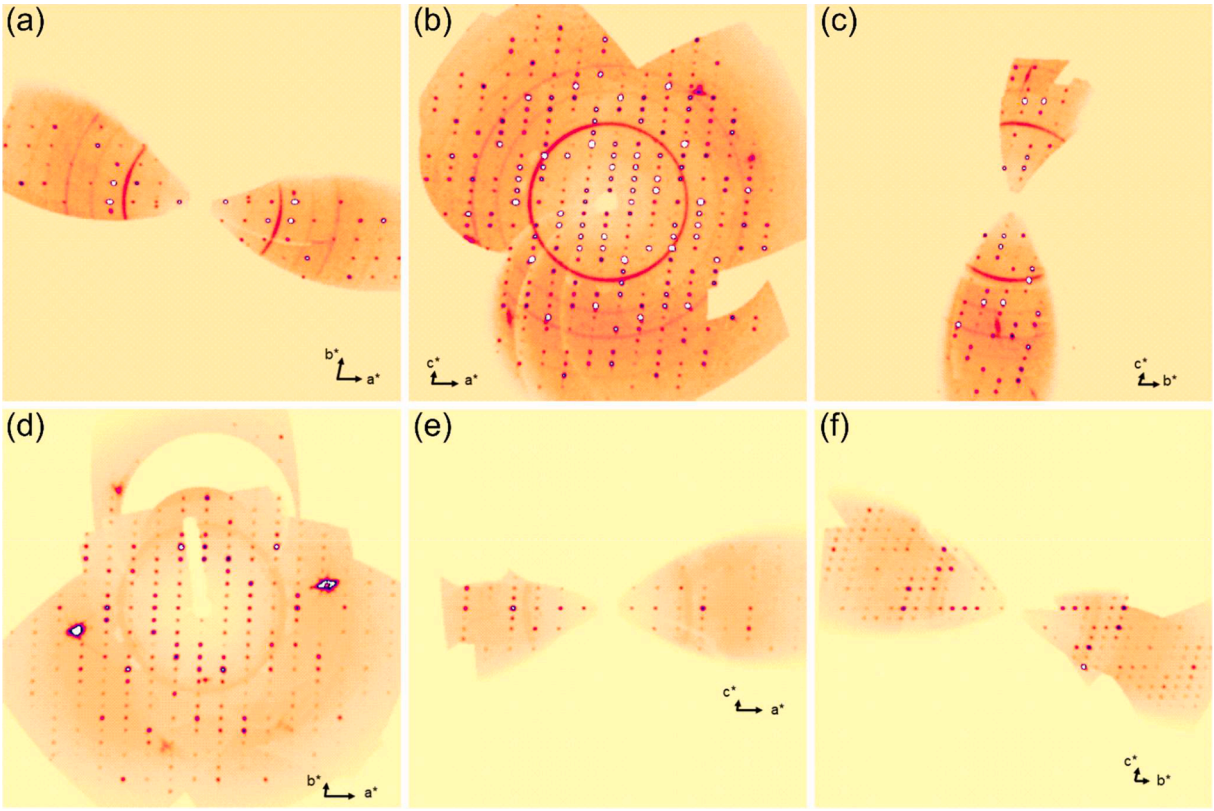

Fig. 2. $Na_3Bi(IO_3)_6$ reciprocal-space precession images constructed from single-crystal X-ray diffraction data. (a-c) The low pressure structure, α-$Na_3Bi(IO_3)_6$, at 1.45 GPa. (d-f) The high pressure structure, β-$Na_3Bi(IO_3)_6$, at 10.07GPa. Saturated reflections (white) correspond the diamond anvils of the DAC. The Debye-Scherrer rings originate from the stainless-steel gasket surrounding the sample.

β-$Na_3Bi(IO_3)_6$ crystal structure of is described for the first time in this publication. At 9.5 GPa the diffraction data of β-$Na_3Bi(IO_3)_6$ phase were integrated with a very low $R_{int} = 0.0462$ for 2812 unique reflections. The reflections were indexed to a triclinic lattice with unit-cell dimensions of: $a = 6.7545(4)$ Å, $b = 13.5350(9)$ Å, $c = 16.288(2)$ Å, $\alpha = 104.895(10)^\circ$, $\beta = 93.952(11)^\circ$, $\gamma = 91.515(6)^\circ$ and $V = 1434.2(3)$ Å^3 at 9.52 GPa. Details of the XRD data collection and refinement for β-$Na_3Bi(IO_3)_6$ are provided in Supplementary Table 6. Reconstructed reciprocal-space precession images for both phases are shown in Fig. 2. Both α-and β-structures are characterised by layers of polyhedra following stacking sequence (IO_3, NaO_x, IO_3, BiO_x, …). The layers of NaO_x and BiO_x are interconnected by IO_3 pyramids. In α-$Na_3Bi(IO_3)_6$ the layers are oriented perpendicular to the crystallographic *b*-axis as shown by the purple (02–1) planes in Fig. 1d and 1e. The effective coordination of the sodium atoms Na1 and Na3 (see Fig. 1a) increases gradually from around 5 to around 6 between 0 GPa and the transition pressure at 9 GPa. The effective coordination of Na2 stays relatively constant around 6, while that of Bi1 increases gradually from 6.5 at ambient pressure to almost 7 after the phase transition (see Fig. 1c). At ambient pressure none of the MO_x polyhedra (M = Na, Bi) share mutual edges, and they only corner-share with IO_3 units. The pressure induced increase in coordination results in edge-sharing of BiO_x and NaO_x polyhedra in the β-phase which is not exhibited in the α-phase. Also, in the α-phase the IO_3 units only corner-share with the NaO_x and BiO_x polyhedra, however, in the β-phase some of them exhibit edge-sharing. Basic crystallographic information for both α-and β-$Na_3Bi(IO_3)_6$ structures is presented in Table 1.

In addition to the results of single crystal XRD, the α-and β-$Na_3Bi(IO_3)_6$ structures were investigated via DFT calculations and polycrystalline (powder) XRD. In particular, the relative stability of the two phases at high pressures was investigated as shown by the relative enthalpy plot shown in Fig. 3a. The $\alpha \rightarrow \beta$ phase transition pressure, according to the single crystal XRD experiments, is 9.2 GPa. According to the DFT calculations the β-phase becomes the more stable phase above 9.25 GPa, in excellent agreement with the experimental results. Additionally, the calculated evolution of the lattice parameters (next section) shows also excellent agreement between experiment and calculation (see Fig. 3b – 3d).

Pressure evolution of lattice parameters and compressibility

The crystal lattice parameters, as determined from the high-pressure single crystal XRD experiments, are plotted in Fig. 3 (solid symbols). The volume per formula unit plotted as function of pressure for both α-and β-$Na_3Bi(IO_3)_6$ phases is shown in Fig. 3b. The data for the low pressure (α) phase were fitted with a 3rd order Birch-Murnaghan (BM) equation of state (EoS), resulting in converged parameters of: $V_0 = 437.4(4)$ Å^3/*Z*, $B_0 = 30.4(7)$ GPa, $B_0' = 6.3(2)$. Exactly the same values were also obtained using the PASCal calculator[28]. The EoS was constrained to second order (i.e. $B_0' = 4$) for the high pressure (β) phase because only 3 data points were recorded. The determined ambient pressure volume and bulk modulus are as follows: $V_0 = 406(2)$ Å^3/*Z* and $B_0 = 59(3)$ GPa, however, due to the very low number of data points for the high pressure phase these values should only be used as a first approximation. The calculated DFT data are in excellent agreement with the experimental data regarding the pressure evolution of the volume and lattice parameters, except for a 1% underestimation of the total volume (see Fig. 3, solid lines). Such small difference is normal for DFT calculations. The experimentally determined volume and lattice parameters determined from the powder XRD data are also shown in Fig. 3 (open symbols). These data were also fitted with a 3rd order BM EoS, resulting in converged parameters of: $V_0 = 442.(2)$ Å^3/*Z*, $B_0 = 26(3)$ GPa, $B_0' = 8(1)$, which is in excellent agreement with the EoS determined from the single crystal XRD. Above the phase transition pressure, ~ 9 GPa, the powder sample became a multi-phase sample of both α-and β-phases, therefore, and in addition to the fact that both crystal structures have triclinic symmetry, it was not possible to determine the lattice parameters of either phase above 9 GPa. The fact that phase coexistence was only observed in powder XRD experiments suggests that it likely originates only from stress between grains in powder experiments, which in turn highlights the importance of single crystal experiments[29]. Importantly, both single crystal and powder XRD measurements do not show any evidence of a phase transition at 2 GPa as previously suggested in Ref. 7.

Table 1
Basic crystal data for α-and β-$Na_3Bi(IO_3)_6$ based on single crystal XRD. Comprehensive experimental crystallographic information is provided in Supplementary Tables 1-6.

Phase	α-$Na_3Bi(IO_3)_6$		β-$Na_3Bi(IO_3)_6$	
Data	Experiment	DFT	Experiment	DFT
Pressure (GPa)	0.0	0.0	9.5	9.5
Crystal System	Triclinic	Triclinic	Triclinic	Triclinic
Space Group	*P*-1	*P*-1	*P*1	*P*1
a (Å)	7.1986(5)	7.1329	6.7545(4)	6.66815
b (Å)	8.9048(4)	8.8062	13.535(9)	13.49488
c (Å)	14.4889(9)	14.4281	16.288(2)	16.18636
α (°)	105.46(5)	106.15372	104.895(1)	105.12566
β (°)	94.564(5)	94.56926	93.952(11)	94.46138
γ (°)	99.325(5)	99.81284	91.515(6)	91.64822
V (Å^3)	875.94(9)	850	1434.2(3)	1400
Z	2	2	4	4

Table 2
Compressibility data for α-$Na_3Bi(IO_3)_6$ determined using data from single crystal XRD only. The principal compression axes (X_1, X_2 and X_3) are represented by black arrows in Fig. 1a. The data in the table were calculated using the lattice parameters from the single crystal XRD analysis (Supplementary Tables 1-6) and the PASCal principal axis strain calculator[28]. Not enough data points were acquired to perform a reliable analysis for the high pressure β-$Na_3Bi(IO_3)_6$ phase.

α-$Na_3Bi(IO_3)_6$ Axis	Compressibility, *K* (GPa^{-1})	Direction [*u v w*]	Approx. direction (*x,y, z*)
X_1	$7.9(1) \times 10^{-3}$	0.9518, −0.1477, −0.2689	10, −1, −3
X_2	$4.43(7) \times 10^{-3}$	0.0102, −0.9771, 0.2126	0, −5, 1
X_3	$4.36(5) \times 10^{-3}$	−0.6829, −0.5323, −0.5003	−7, −5, −5

According to the normalised lattice parameters as a function of pressure (shown in Fig. 3c) in the low-pressure phase, the crystallographic *a*-axis is the most compressible, as seen by the quicker deviation from its ambient pressure value. This observation is supported by the principal compression axes which are reported in Table 2. The softest of the principal compression axes, X_1, is approximately parallel with the *a*-axis because it points in the [10,–1,–3] direction, which has a large *a* component. X_1 has a compressibility of $7.9(1) \times 10^{-3}$ GPa^{-1}, making it twice as compressible as the other two principal axes (4.43(7) and 4.36 (5) $\times$ 10^{-3} GPa^{-1}), and making α-$Na_3Bi(IO_3)_6$ an anisotropically compressible material. This similar compressibilities of X_2 and X_3 is also mirrored by the similar behaviour of the *b* and *c* axes in Fig. 3b, although the reader should note that the crystallographic axes and the principal compression axes are only equivalent in crystal systems where the crystal axes are orthogonal (cubic, tetragonal or orthorhombic). The excellent agreement between experiment and theory is also seen in the behaviour of the unit cell angles (Fig. 3c). We find that the angle α increases with pressure, whereas the other two angles, β and γ, both decrease with pressure.

Electronic structure

The bandgap of $Na_3Bi(IO_3)_6$ as a function of pressure was determined by single crystal UV–vis transmission spectroscopy and by DFT calculations (more details in Section 2.2). At ambient pressure the indirect bandgap was measured at 3.64(5) eV (3.09 eV) in experiment (calculations), which falls within the UV region of the electromagnetic

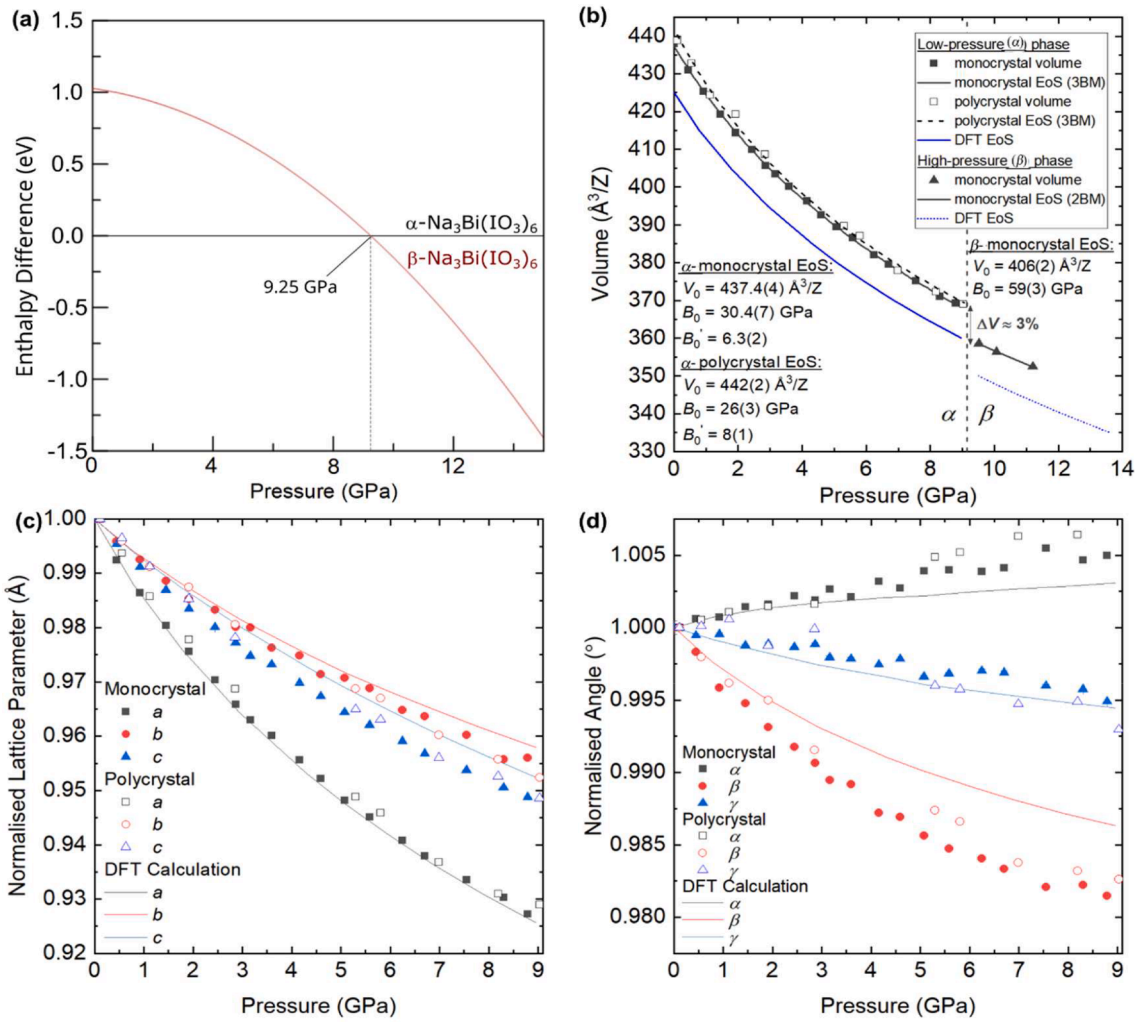

Fig. 3. Pressure induced evolution of α-and β-$Na_3Bi(IO_3)_6$ enthalpy and crystal lattice parameters. (a) Calculated enthalpy for the triclinic α-$Na_3Bi(IO_3)_6$ (P-1) and the triclinic β-$Na_3Bi(IO_3)_6$ ($P1$) phases. The enthalpy of the low pressure α-$Na_3Bi(IO_3)_6$ phase is taken as reference. (b) Volume per formula unit, (c) normalised lattice parameters, and (d) normalised unit cell angles as functions of pressure. Solid (open) symbols correspond to monocrystal (polycrystal) XRD measurements.

spectrum. The measured bandgap as a function of pressure is shown in Fig. 4a. Selected experimental absorption spectra are shown in Fig. 4b. The bandgap closes with increasing pressure. Between 11.1 and 11.7 GPa a sudden bandgap decrease of 0.07 eV occurs, corresponding to the $\alpha \rightarrow \beta$ phase transition. The transition pressure observed in this optical absorption experiment (11.4 GPa) is higher than the transition pressure observed in the XRD experiments (9.2 GPa). This is a common observation in optical experiments, since the decreased bandgap of the high-pressure phase only starts to dominate the absorption behaviour of the sample once a sufficiently large fraction of material has transitioned to the new phase.

The calculated bandgap as a function of pressure is shown in Fig. 4c. Whilst the absolute calculated values of the calculated bandgaps are lower than those observed in experiment, there is good agreement between experiment and theory regarding the pressure evolution and regarding the bandgap difference between the α- and β- phases. In both experiment and calculations, the bandgap also continues to decrease with pressure in the HP phase up to the maximum pressures observed. The displayed transition pressure is based on that observed in the XRD experiments and predicted by the DFT enthalpy calculations (see Fig. 3a and 3b). The underestimation of the bandgap by DFT is a common result related to the approximations used to describe the exchange and correlation energies in the GGA-AM05 description[30]. However, this description provides an accurate description of changes induced by pressure in the bandgap. The decreasing bandgap energy is concurrent with an increase in the average I-O bond length, as shown in Fig. 4d. This is consistent with observations from other works[31]. Across the α to β phase transition the average I-O bond distance also jumps to larger values, consistent with the sudden decrease in the bandgap energy. According to the DFT calculations of Ref. 7, the bottom of the conduction band is mainly contributed to by I and O orbitals, thereby reinforcing the notion that the I-O bond distance plays a key role in the optical properties of iodate materials.

In Ref. 7 the authors determine the indirect bandgap of α-$Na_3Bi(IO_3)_6$ to be 3.21 eV at ambient pressure, which is in general agreement with our experimental (3.64(5) eV) and calculated results (3.09 eV, see Fig. 5). In Ref. 7 the bandgap of α-$Na_3Bi(IO_3)_6$ was estimated by powder UV–vis diffuse-reflectance spectroscopy, which tends to underestimate the bandgap energy due to unwanted transmission of light[32]. In the current work, the bandgap of α-$Na_3Bi(IO_3)_6$ was estimated by single crystal UV–vis transmission spectroscopy which does not have the same disadvantage. By comparing the band structures of the low- and high-pressure phases we can see there is a change in the topology of the band structure at the phase transition. In the low-pressure phase the valence band has a very low dispersion. In contrast, in the HP phase the valence band is much more dispersive. This indicates that at the phase transition there is an increase of the overlap / hybridization of the states near the Fermi energy. In $Na_3Bi(IO_3)_6$ these states are mainly

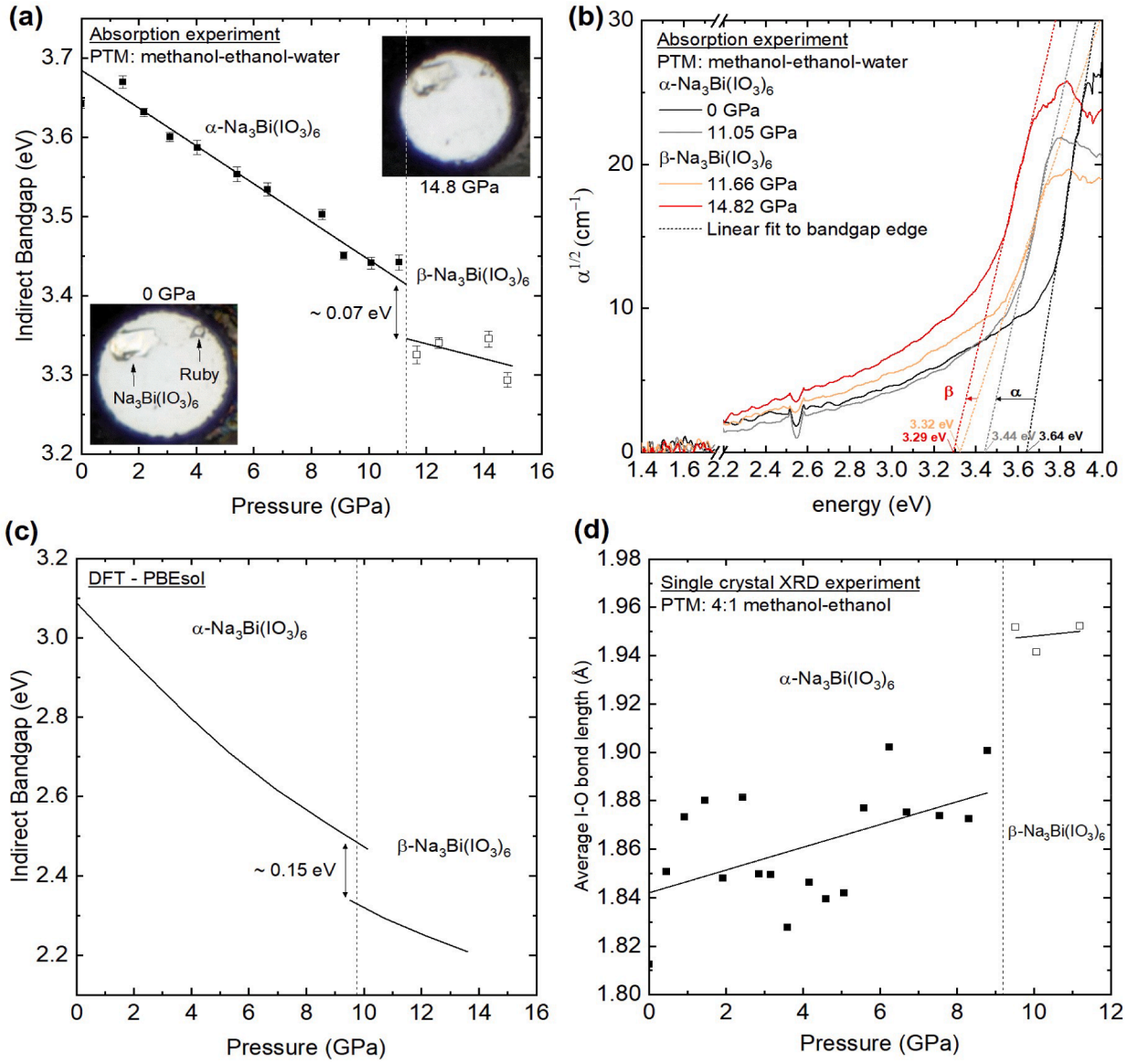

Fig. 4. $Na_3Bi(IO_3)_6$ bandgap evolution with pressure according to experiment and DFT calculations. $Na_3Bi(IO_3)_6$ indirect bandgap as a function of pressure determined from (a) single crystal absorption spectroscopy. (b) Selected experimental Tauc plots showing the lowest and highest pressures observed for the α- and β-phases. The spectra and linear fits for all pressures are shown in Supplementary Figs. 2 and 3. (c) $Na_3Bi(IO_3)_6$ bandgap as a function of pressure according to DFT calculations. (d) Average I-O bond length as a function of pressure.

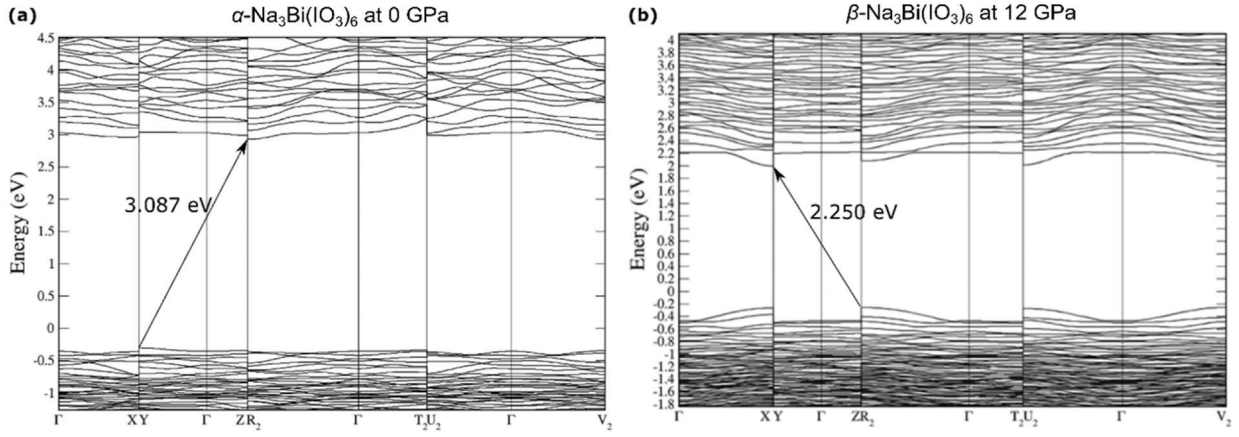

Fig. 5. The band structures of α- and β-$Na_3Bi(IO_3)_6$ at 0 and 12 GPa respectively. Both α- and β-phases exhibit indirect band structures as indicated by arrows.

contributed to by the O-2p and I-5p orbitals. In the low-pressure phase, the IO_3 molecules are isolated from equivalent molecules and therefore interactions between neighbouring iodate units will be small (and consequently orbital overlap between O-2p and I-5p states from neighbouring iodate units will also be small), leading to the reported flat bands. In contrast, in the HP phase, due to the volume collapse and structural reorganization, iodate molecules are much closer to each other, thereby enhancing the interaction among first neighbouring IO_3 units and increasing the widths of the bands. This fact explains not only the increase of the bands dispersion but also the decrease of the band-gap energy.

Conclusions

In this work we have performed a combined experimental / theoretical high-pressure study of $Na_3Bi(IO_3)_6$ under compression to 11.2 GPa at ambient temperature. Through a combination of single-crystal and powder synchrotron X-ray diffraction, single-crystal optical absorption measurements and *ab initio* density functional theory calculations we have unambiguously shown a first-order pressure-induced phase transition around 9.5 GPa from α-$Na_3Bi(IO_3)_6$ to a new crystalline structure referred to here as β-$Na_3Bi(IO_3)_6$. The crystal structures of both phases are reported here. The relative stability of both phases at high pressure was investigated by DFT calculations, which found the β-phase to be more stable above 9.25 GPa, in excellent agreement with experiment. The triclinic (P-1) to triclinic (P1) phase transition is characterised by a doubling of the primitive cell volume, whereby the crystallographic b-axis doubles in length, and by a decrease in the volume per formula unit of approximately 3 %. The phase transition is also characterised by an indirect → indirect electronic bandgap decrease of approximately 0.1 eV as measured by absorption spectroscopy (3.44(1) → 3.32(1) eV), in general agreement with density functional calculations (2.48 → 2.33 eV). The pressure evolution of the crystal lattice parameters and isothermal compressibility tensor of the ambient pressure phase α-$Na_3Bi(IO_3)_6$ are reported, which reveal highly anisotropic compressibility and a bulk modulus of 30.4(7) GPa.

Finally, although the α- and β-$Na_3Bi(IO_3)_6$ crystal structures are unambiguously determined in this work by XRD, thereby demonstrating conclusively that the α-$Na_3Bi(IO_3)_6$ phase exists from 0.0 to 8.9 GPa, it is necessary to include a discussion of the previous findings of Ref. 7 in which they claim to observe a pressure-induced phase transition in α-$Na_3Bi(IO_3)_6$ at 1.9 GPa based on high-pressure Raman spectra, stating, "With increasing pressure to 1.9 GPa, two new Raman peaks are emerged at 769 and 709 cm^{-1}." There are two important points to make about these modes (shown in Supplementary Fig. 4). Firstly, these two Raman modes respectively coincide with the CH_3 rocking and SiC_2 antisymmetric stretching modes from the silicone oil [33,34] which was used as a pressure transmitting medium in Ref. 7. Secondly, it is important to consider overlap of with other modes from α-$Na_3Bi(IO_3)_6$. For example, the lower frequency mode around 709 cm^{-1} from SiC_2 overlaps perfectly with a vibrational mode from the sample, until the sample mode red-shifts to lower energies due to increasing pressure, thereby revealing the SiC_2 mode. Similarly, the higher frequency mode around 769 cm^{-1} from CH_3, is hidden in the shoulder of a sample mode at pressures lower than 1.9 GPa.

Data availability

All relevant data are available from the corresponding author upon reasonable request. Supplementary crystallographic data for both α-and β-$Na_3Bi(IO_3)_6$ structures can be obtained free of charge from the Cambridge Crystallographic Data Centre (CCDC) under deposition numbers: 2162824–2162844.

CRediT authorship contribution statement

Robin Turnbull: Conceptualization, Methodology, Investigation, Formal analysis, Writing – original draft, Visualization, Funding acquisition. **Javier González-Platas:** Investigation, Formal analysis, Writing – review & editing, Visualization. **Akun Liang:** Investigation. **Dequan Jiang:** Investigation. **Yonggang Wang:** Investigation. **Catalin Popescu:** Investigation. **Plácida Rodríguez-Hernández:** Investigation, Formal analysis, Writing – review & editing. **Alfonso Muñoz:** Investigation, Formal analysis, Writing – review & editing. **Jordi Ibáñez:** Investigation, Writing – review & editing. **Daniel Errandonea:** Conceptualization, Formal analysis, Writing – review & editing, Funding acquisition.

Declaration of Competing Interest

The authors declare that they have no known competing financial interests or personal relationships that could have appeared to influence the work reported in this paper.

Data availability

Data will be made available on request.

Acknowledgements

The authors acknowledge financial support from the Spanish Research Agency (AEI) and Spanish Ministry of Science and Investigation (MCIN) under projects PID2019106383GB-C41/C43/C44 (DOI: 10.13039/501100011033), and projects PGC2018-101464-B-I00 and PGC2018-097520-A-I00 (cofinanced by EU FEDER funds). The authors acknowledge financial support from the MALTA Consolider Team network, under project RED2018-102612-T and from Generalitat Valenciana under Grant No. PROMETEO CIPROM/2021/075-GREENMAT. R.T. acknowledges funding from the Spanish Ministry of economy and competitiveness (MINECO) via the *Juan de la Cierva Formación* program (FJC2018-036185-I) and the Generalitat Valenciana for the postdoctoral Fellowship No. CIAPOS/2021/20. J.G.P. thanks the *Servicios Generales de Apoyo a la Investigación* (SEGAI) at the University of La Laguna. A.L. and D.E. would like to thank the *Generalitat Valenciana* for the Ph.D. fellowship GRISOLIAP/2019/025. This study forms part of the Advanced Materials programme (Grant MFA/2022/007) and was supported by MCIN with funding from European Union NextGenerationEU (PRTR-C17.I1) and by Generalitat Valenciana. The authors also thank ALBA synchrotron light source for funded experiment under proposal number 2021085271 at the MSPD-BL04 beamline. The authors thank J. Sanchez-Martin for assistance in powder XRD measurements.

Appendix A. Supplementary data

Supplementary data to this article can be found online at https://doi.org/10.1016/j.rinp.2022.106156.

References

[1] Gai M, Tong T, Wang Y, Yang Z, Pan S. New Alkaline-Earth Metal Fluoroiodates Exhibiting Large Birefringence and Short Ultraviolet Cutoff Edge with Highly Polarizable $(IO_3F)^{2-}$ Units. Chem Mater 2020;32:5723–8. https://doi.org/10.1021/acs.chemmater.0c01452.

[2] Zhang J, Du X, Ke SH, Xu B, Zheng G, Rowlands DA, et al. Dielectric, piezoelectric and nonlinear optical properties of polar iodate $BiO(IO_3)$ from first-principles studies. J Solid State Chem 2020;281:121057. https://doi.org/10.1016/j.jssc.2019.121057.

[3] Liu H, Jiang X, Wang X, Yang L, Lin Z, Hu Z, et al. Influence of A-site Cations on Germanium Iodates as Mid-IR Nonlinear Optical Materials: $A_2Ge(IO_3)_6$ (A = Li, K, Rb and Cs) and $BaGe(IO_3)6H_2O$. J Mater Chem C 2018;6:4698–705. https://doi.org/10.1039/C8TC00851E.

[4] Huang H, He Y, Guo Y, He R, Lin Z, Zhang Y. Hydrothermal synthesis, nonlinear optical property and photocatalytic activity of a non-centrosymmetric $AgIO_3$

photocatalyst under UV and visible light irradiation. Solid State Sci 2015;46:37–42. https://doi.org/10.1016/j.solidstatesciences.2015.05.008.
[5] Mao FF, Hu CL, Xu X, Yan D, Yang BP, Mao JG. $Bi(IO_3)F_2$: the first metal iodate fluoride with a very strong second harmonic generation effect. Angew Chem 2017; 129:2183–7. https://doi.org/10.1002/anie.201611770.
[6] Cao Z, Yue Y, Yao J, Lin Z, He R, Hu Z. $Bi_2(IO_4)(IO_3)_3$: A new potential infrared nonlinear optical material containing $[IO_4]^{3-}$ anion. Inorg Chem 2011;50: 12818–22. https://doi.org/10.1021/ic201991m.
[7] Song H, Jiang D, Wang N, Xing W, Guo R, Lin Z, et al. $Na_3BiIO_3)_6$: An Alkali-Metal Bismuth Iodate with Intriguing One-Dimensional $[BiI_6O_{18}]$ Chains and Pressure-Induced Structural Transition. Inorg Chem 2021;60(5):2893–8. https://doi.org/10.1021/acs.inorgchem.0c03697.
[8] Rigaku Oxford Diffraction - CrysAlisPro Software system, version 1.171.41.99a. *Rigaku Corporation, Oxford, UK* (2021). No DOI available.
[9] Angel R, Gonzalez-Platas J. Absorp-7 and Adsorb-GUI for single-crystal absorption corrections. J Appl Crystallogr 2013;46:252–4. https://doi.org/10.1107/S0021889812048431.
[10] Klotz S, Chervin J-C, Munsch P, Le Marchand G. Hydrostatic limits of 11 pressure transmitting media. J Phys D 2009;42(7). https://doi.org/10.1088/0022-3727/42/7/075413.
[11] Shen G, Wang Y, Dewaele A, Wu C, Fratanduono DE, Eggert J, et al. Toward an international practical pressure scale: A proposal for an IPPS ruby gauge (IPPS-Ruby2020). High Press Res 2020;40(3):299–314.
[12] Sheldrick GM. Crystal structure refinement with SHELXL. Acta Crystallogr C: Struct Chem 2015;71:3–8. https://doi.org/10.1107/S2053229614024218.
[13] Fauth F, Peral I, Popescu C, Knapp M. The new material science powder diffraction beamline at ALBA synchrotron. Powder Diffr 2013;28:S360–70. https://doi.org/10.1017/S0885715613000900.
[14] Tauc J. Optical properties and electronic structure of amorphous Ge and Si. Mater Res Bull 1968;3(1):37–46.
[15] Gonzalez-Platas J, Alvaro M, Nestola F, Angel R. EosFit7-GUI: a new graphical user interface for equation of state calculations, analyses and teaching. J Appl Crystallogr 2016;49:1377. https://doi.org/10.1107/S1600576716008050.
[16] Birch F. Finite Elastic Strain of Cubic Crystals. Phys Rev 1947;71:809–24. https://doi.org/10.1103/PhysRev.71.809.
[17] Angel RJ. Equations of state. Rev Mineral Geochem 2000;41(1):35–59.
[18] Hohenberg P, Kohn W. Inhomogeneous electron gas. Phys Rev B 1964;136(3B): B864–71.
[19] Kresse G, Furthmüller J. Efficiency of *ab-initio* total energy calculations for metals and semiconductors using a plane-wave basis set. Comput Mater Sci 1996;6:15–50. https://doi.org/10.1016/0927-0256(96)00008-0.
[20] Kresse G, Furthmüller J. Efficient iterative schemes for *ab initio* total-energy calculations using a plane-wave basis set. Phys Rev B 1996;54(16):11169–86.
[21] Blöchl PE. Projector augmented-wave method. Phys Rev B 1994;50(24):17953–79.
[22] Kresse G, Joubert D. From ultrasoft pseudopotentials to the projector augmented-wave method. Phys Rev B 1999;59(3):1758–75.
[23] Armiento R, Mattsson AE. Functional designed to include surface effects in selfconsistent density functional theory. Phys Rev B 2005;72:085108. https://doi.org/10.1103/PhysRevB.72.085108.
[24] Mattsson AE, Armiento R, Paier J, Kresse G, Wills JM, Mattsson TR. The AM05 density functional applied to solids. J Chem Phys 2008;128(8). https://doi.org/10.1063/1.2835596.
[25] Monkhorst HJ, Pack JD. Special points for Brillouin-zone integrations. Phys Rev B 1976;13:5188. https://doi.org/10.1103/PhysRevB.13.5188.
[26] Hinuma Y, Pizzi G, Kumagai Y, Oba F, Tanaka I. Band structure diagram paths based on crystallography. Comp Mat Sci 2017;128:140. https://doi.org/10.1016/j.commatsci.2016.10.015.
[27] Momma K, Izumi F. VESTA: a three-dimensional visualization system for electronic and structural analysis. J Appl Crystallogr 2008;41:653–8. https://doi.org/10.1107/S0021889808012016.
[28] Cliffe MJ, Goodwin AL. PASCal: a principal axis strain calculator for thermal expansion and compressibility determination. J Appl Crystallogr 2012;45:1321–9. https://doi.org/10.1107/S0021889812043026.
[29] Gonzalez-Platas J, Lopez-Moreno S, Bandiello E, Bettinelli M, Errandonea D. Precise characterization of the rich structural landscape induced by pressure in multifunctional $FeVO_4$. Inorg Chem 2020;59:6623–30. https://doi.org/10.1021/acs.inorgchem.0c00772.
[30] Chan MKY, Ceder G. Efficient Band Gap Prediction for Solids. Phys Rev Lett 2010; 105:196403. https://doi.org/10.1103/PhysRevLett.105.196403.
[31] Liang A, Turnbull R, Rodriguez-Hernandez P, Muñoz A, Jasmine M, Shi LT, et al. General relationship between the band-gap energy and iodine-oxygen bond distance in metal iodates. Phys Rev Mater 2022;6:044603. https://doi.org/10.1103/PhysRevMaterials.6.044603.
[32] Botella P, Errandonea D, Garg AB, Rodriguez-Hernandez P, Muñoz A, Achary SN, et al. High-pressure characterization of the optical and electronic properties of $InVO_4$, $InNbO_4$, and $InTaO_4$. *SN*. Appl Sci 2019;1, Article number: 389. https://doi.org/10.1007/s42452-019-0406-7.
[33] Wang X, Li Z, Chen C, Wang K, Han B, Zhou Q, et al. High Pressure Raman Spectra of Silicone Oil. Chem J Chin Univ 2014;35:2384–9. https://doi.org/10.7503/cjcu20140541.
[34] Chen X, Lou H, Zeng Z, Cheng B, Zhang X, Liu Ye, et al. Structural transitions of 4:1 methanol–ethanol mixture and silicone oil under high pressure. Matter Radiat Extremes 2021;6(3).